JOURNAL OF MATERIALS SCIENCE 28 (1993) 4223–4228

Deposition from the vapour phase during induction plasma treatment of alumina powders

T. ISHIGAKI, Y. BANDO, Y. MORIYOSHI
National Institute for Research in Inorganic Materials, 1-1, Namiki, Tsukuba, Ibaraki 305, Japan

M. I. BOULOS
Plasma Technology Research Centre (CRTP), University of Sherbrooke, Sherbrooke, Quebec, Canada J1K 2R1

A study was carried out of the induction plasma melting of alumina powders (particle mean diameter, $\bar{d}_p = 24.5$ μm), (Ar/H_2 or Ar/N_2 plasma, plate power, 40 kW) under reduced pressure conditions (400 torr). The results reveal that in the process, partial vaporization of the alumina powders takes place in the hot region of the discharge. As the molten particles cool down and solidify, the deposits from the vapour phase was formed with the spheroidized particles. In all treatments with the Ar/H_2 and Ar/N_2 plasmas, a condensate of ultrafine alumina fume ($d_p < 200$ nm) was obtained. The fine particles consisted essentially of metastable γ-, δ- and θ-phases. Needle-like crystals(0.1–0.3 μm diameter, by 5–15 μm long) were observed when operating with an Ar/N_2 plasma at powder feed rates exceeding 10 g min^{-1}. Electron diffraction analysis revealed that the needles were whiskers, whose structure was very similar to κ- or χ-aluminas with an hexagonal close-packed oxygen lattice. The change of morphology is related to the degree of supersaturation in the vapour phase.

1. Introduction

Thermal plasmas generated at 1 atm offer a high-temperature energy source for the thermal treatment of powders. The process has been widely adopted, for example, in the plasma spray coating. Powders injected into the plasma receive a tremendous heat to melt and evaporate in a short time, and then are cooled rapidly. Through this powder processing, the morphology, crystal structure and chemical composition of plasma-treated powder may be modified by controlling the plasma-generating and powder-feeding conditions.

We have carried out a study of the spheroidization of alumina powders in r.f. induction plasmas [1], in which alumina powders were heat treated with Ar/H_2 and Ar/N_2 plasmas. When the hydrogen content is equal to that of nitrogen, the Ar/H_2 plasma has a higher thermal conductivity than the Ar/N_2 plasma. This gives rise to the higher heat-transfer rate from the plasma to the particles [2], in the Ar/H_2 plasma compared to those in the Ar/N_2 plasma. Under such high heat-flux conditions, partial powder vaporization and condensation have been observed. The amount of evaporation and the morphology of deposits from the vapour phase varied depending on the plasma-generating and powder-feeding conditions. In agreement with the numerical prediction [2, 3], a larger amount of spongy mass, i.e. fine spherical particles deposited from the vapour phase, was formed in the Ar/H_2 plasma-treated alumina powders, and the amount increased with decrease in the powder feed rate. In addition, in some powders treated with the Ar/N_2 plasma, a needle-like structure was formed. The needles were observed at the higher powder feed rate, in which less evaporation occurred. The degree of supersaturation in the gas phase under these conditions was relatively low, when the plasma was cooled in the tail region.

In the growth from the vapour phase, the supersaturation in the vapour phase has an important effect on the nucleation rate and the growth form. It is known that the driving force for condensation from the gas phase at the temperature, T, with the pressure, P, is the free-energy difference, $\Delta\mu$

$$\Delta\mu = -kT\ln(P/P_e) = -kT\ln\alpha \quad (1)$$

where P_e is the pressure in equilibrium, and α is the saturation ratio (α-1 is the supersaturation) [4]. As alumina particles pass through a high-temperature region exceeding 10 000 K, the vapour pressure of evaporated species is very large, and the degree of supersaturation increases considerably when the plasma is cooled, resulting in the homogeneous nucleation in the vapour phase. Because the temperature drops very rapidly outside the plasma, the coalescence

0022–2461

is suppressed and very fine powders are obtained. There have been many reports concerning the synthesis of alumina fine powders, e.g. by the oxidation of aluminium chloride [5, 6] and the pyrolysis of aluminium nitrate aqueous solution [7] in thermal plasmas such as r.f. and d.c. arcs.

The reported alumina fine powders consisted of metastable γ-, δ- and θ-phases. Alumina has a wealth of metastable phases. They are generally prepared by calcination of aluminium hydroxides following the decomposition reactions [8]

$$\begin{array}{lllllllll} \text{Gibbsite} & \rightarrow & \chi & \rightarrow & \kappa & \rightarrow & \alpha & & \\ & \searrow & & & & & & & \\ & & \text{Boehmite} & \rightarrow & \gamma & \rightarrow & \delta & \rightarrow & \theta & \rightarrow & \alpha \\ & \nearrow & & & & & & & \\ \text{Bayerite} & \rightarrow & \eta & \rightarrow & \theta & \rightarrow & \alpha & & \\ & & & & & & & & \\ & & \text{Diaspore} & & \rightarrow & & \alpha. & & \end{array} \quad (2)$$

It is known that the formation of metastable phases depends on the calcination condition, such as thermal history and reaction atmosphere.

In this paper, the alumina deposition from the vapour phase is discussed during the in-flight powder treatment. Variation in the deposits furnishes information of the environment around the melted particles in thermal plasmas, and the information greatly contributes to the knowledge of the interaction between plasma and particles.

2. Experimental procedure

The apparatus used in this experiment has been reported previously [1]. The plasma was generated using a radio-frequency power supply with a nominal oscillator frequency of 3 MHz and a maximum plate power of 50 kW. Three gas streams were introduced into the torch. The operating conditions are summarized in Table I. The plasma is confined in a 50 mm inner diameter (i.d.) water-cooled quartz tube. The plasma discharges, at the end of the confinement tube, into a water-cooled stainless steel chamber with an i.d. of 254 mm and a length of 1020 mm.

α-alumina powder [AMDRY, PWA 1310E] with a mean diameter of 24.5 μm and a standard deviation of 6.0 μm was axially injected into the centre of the discharge.

TABLE I Plasma-generating parameters and powder-feeding conditions

Sheath gas (1)	Ar	Ar
(l min^{-1})	82	82
Sheath gas (2)	H_2	N_2
(l min^{-1})	9.6	9.6
Plasma gas	Ar	Ar
(l min^{-1})	28	28
Powder carrier gas	Ar	N_2
(l min^{-1})	6.9	6.9
R.f. frequency (MHz)	3	
Plate power (kW)	40	
Reactor pressure (torr[a]):	400	
Powder feed rate (g min^{-1})	1–50	

[a] 1 torr = 133.322 Pa.

The alumina powders, which passed through the plasma, were collected separately at the reactor wall, reactor bottom, cyclone and filter. The collected powders were observed with a scanning electron microscope (SEM, Akashi ISI-DS130) equipped with an energy dispersive X-ray spectroscope (EDX, EDAX PV9900). For transmission electron microscopy (TEM), powders were dispersed in ethanol and were placed on to copper grids, and observed by a Hitachi H-500 and a JEOL JEM-2000EX electromicroscopes, operated at 100 kV.

3. Results

Particles introduced into the plasma were heated to melt and evaporate. In the Ar/H_2 plasma treatment, and the Ar/N_2 plasma treatment at the lower powder feed rate, the spongy mass was formed on the surface of the spheroidized large particles as shown in Fig. 1a. The needle-like structure on the particles was observed at the powder feed rate of 10–50 g min^{-1} in the Ar/N_2 plasma treatment, in which the amount of evaporation was relatively small. At the higher feed rate, only needles were formed on the large particles (Fig. 1c). EDX analysis revealed that the whiskers do not include any metal impurities. Fig. 1b is an intermediate feature, that is, the co-deposition of spongy mass and needles.

Fig. 2a is a transmission electron micrograph of the spongy mass, which consists of fine particles of less than some hundreds of nanometres in diameter. Most of them are spherical but some larger particles showed crystal habits, such as an octahedron. An electron diffraction pattern from the fine particles (Fig. 2b) indicates that they consist of γ-, δ- and θ-aluminas. These were weak against electron-beam irradiation with a high current intensity, and easily transformed to α-alumina.

Fig. 3a is a transmission electron micrograph of the needle-like crystal. The needles are 0.1–0.3 μm diameter and 5–15 μm long, and their surface is covered with very fine particles of some tens of nanometres in diameter. The bonding between a crystal and fine particles was so strong that it was difficult to separate them by ultrasonic vibration in ethanol. An electron diffraction pattern is inset on the left-hand side. The incident electron beam was in the direction perpendicular to the axis of the needle. The streaking of diffraction spots normal to the incident beam is observed. Indices of the diffraction pattern are shown in Fig. 3b.

4. Discussion

4.1. Ultra-fine particles

Suzuki *et al.* [9] synthesized many kinds of oxide fine powders by spray pyrolysis of aqueous salt solutions in r.f. induction plasma. From the observation of fine particles, they concluded that at an early stage of crystal growth from the gas phase the particle morphology reflects the crystal structure. Their fine powders had diameters ranging from 15–35 nm, and the shape of the oxides with monoclinic structure was

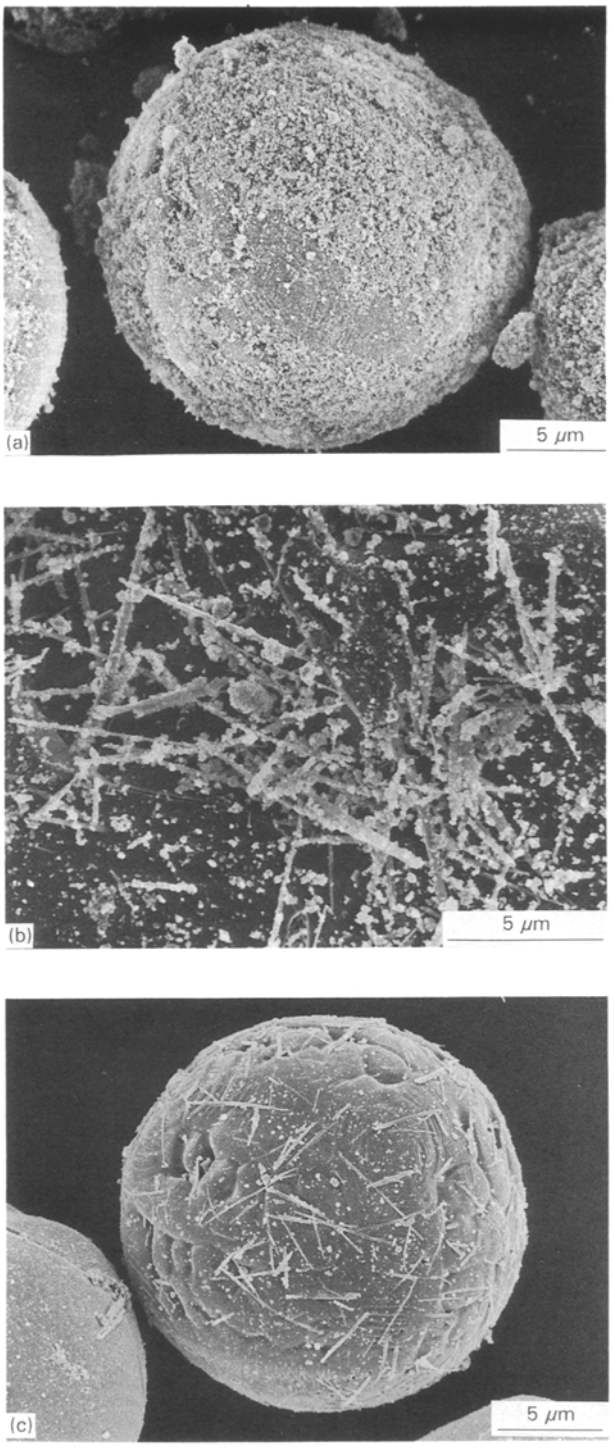

Figure 1 Scanning electron micrographs of Ar/N_2 plasma-treated powders. Powder feed rate: (a) 5 g min^{-1}, (b) 18 g min^{-1}, (c) 50 g min^{-1}.

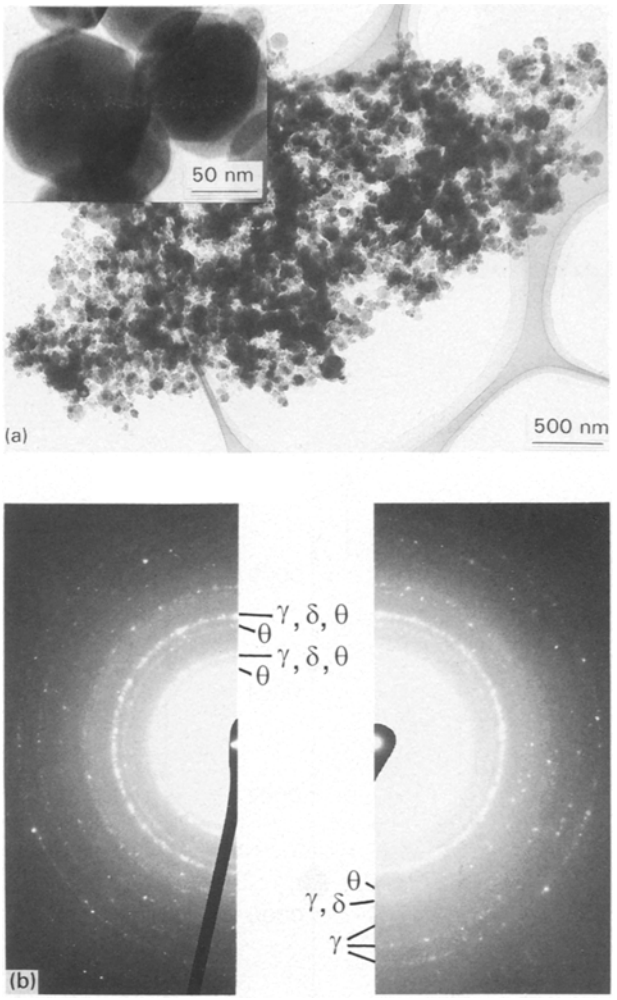

Figure 2 Fine spherical particles deposited in Ar/H_2 plasma treatment (powder feed rate 6 g min^{-1}). (a) TEM image, and (b) electron diffraction pattern. In the photograph inset at the left-hand side of (a), faceted polyhedrons are shown. Indexes of the diffraction pattern are as follows: θ (1 1 1); γ (4 0 0), δ (4 0 0), θ (0 0 6, 2 1 1); θ (3 1 $\bar{3}$); γ (1 0 0), δ (4 0.1 2), θ (2 1 5, 2 1 7); θ (1 2 4); γ (4 4 4), θ (4 4.1 2); γ (8 0 0); γ (8 4 0); γ (8 4 4).

spherical. Some of the oxides with cubic and tetragonal lattices were also spherical.

γ-, δ-, and θ-aluminas have cubic, tetragonal and monoclinic structure, respectively. Most of the alumina fine particles formed in the present work were also spherical. However, some particles were faceted polyhedrons as shown in the micrograph inset on Fig. 2a. The faceted fine particles of γ-, δ- and θ-aluminas were also detected by high-resolution TEM study, in which the fine spherical particles were prepared by the reaction of evaporated aluminium in argon and oxygen gases and whose diameter was between 5 and 100 nm [10].

The nucleation and following coalescence growth depends strongly on the vapour pressure of evaporated species. Fig. 4 is the equilibrated composition for the Al_2O_3 powders in an Ar/H_2 plasma obtained by minimization of the Gibbs free energy [11]. In the figure, the vapour pressure of the species evaporated from alumina such as aluminium, AlO, Al_2O, oxygen and OH shows a steep decrease below the boiling point of alumina. As alumina particles pass through the high-temperature region exceeding 10000 K, the vapour pressures of gas species evaporated from alumina are much greater than the equilibrated ones with liquid alumina, that is, the degree of supersaturation is considerably higher. According to the theory of homogeneous nucleation, the free energy of formation of a stationary spherical cluster in a large volume of vapour is given by

$$\Delta G(r) = -(4\pi r^3 \Delta\mu/3v) + 4\pi r^2\sigma \qquad (3)$$

where r is the radius of the cluster, v the molecular volume, σ the specific surface energy [12]. When the value of $\Delta\mu$ is large, i.e. under high supersaturation, the critical radius, $r^*(=2v\sigma/\Delta\mu)$ becomes smaller.

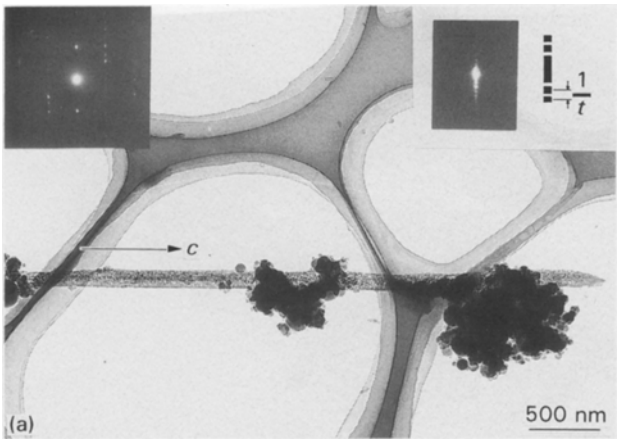

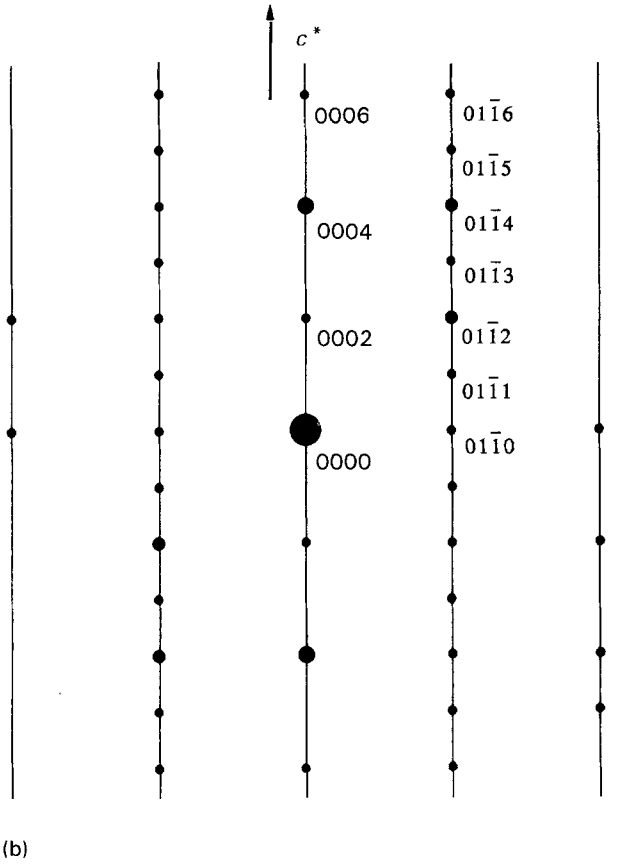

Figure 3 (a) TEM of the deposit in Ar/N_2 plasma treatment (powder feed rate 12 g min^{-1}). Selected-area electron diffraction pattern of the needle-like structure is inset in the left-hand side. Indices of the electron diffraction pattern are shown in (b), where the incident direction of the electron beam is assumed to be [1 0 $\bar{1}$ 0] of hexagonal structure. The pattern shows streaks in the direction of the c^*-axis, and the thickness of the thin section is estimated from the interval between the spikes inset in the right-hand side of (a). The spikes are the enlargement of a diffraction spot.

Over the value of r^*, the cluster spontaneously grows larger. Also, the critical free energy, G^*, for the cluster with r^* is lowered.

Under conditions with a large value of $\Delta\mu$, the nucleation and subsequent coalescence of alumina would occur as the liquid phase. Then, the solidification of liquid droplets follows, as analysed previously [13]. It was concluded that homogeneous nucleation during the solidification of liquid droplets at considerable undercooling resulted in the formation of γ-alumina rather than α-alumina because of its

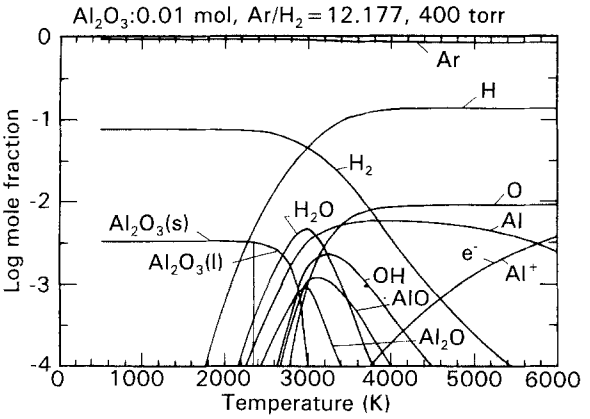

Figure 4 Equilibrated composition for the Al_2O_3–Ar–H_2 system.

lower critical free energy of nucleation. The two intermediates, δ and θ, in the transformation series from γ to α are formed during the solidification exotherm in the tail flame region.

4.2. Whiskers

The intervals between the rows of streaking spots and each spot parallel to the streaking row correspond to the lattice spacings, $d = 0.487$ and 1.72 nm, respectively. The compounds such as aluminium oxides, aluminium hydroxides and aluminium oxynitrides were taken into consideration to compare the unit cell dimension. As is shown in Table II, the unit cell dimension of the present whisker is close to those of χ- and κ-aluminas: $a = 0.557$ nm, $c = 0.864(1.72/2)$ nm [17], $a = 0.971$ nm, $c = 1.786$ nm [16].

It is known that both χ- and κ-aluminas have the hexagonal close-packed (h c p) oxygen sublattice like α-alumina. Okumiya *et al.* reported the transformation series [18] Tohdite → κ′ → κ → α. Tohdite with the hexagonal lattice was prepared by the hydrothermal treatment of η-alumina or Gibbsite. The crystal structure of Tohdite was precisely studied to determine the space group, atom positions and unit cell dimensions [20]. It was also suggested that during transformation from Tohdite to κ′-alumina the oxygen layers remained unchanged. The unit cell of κ′-alumina on the basal (0 0 0 1) plane of hexagonal lattice is shown in Fig. 5. Recently, Liu and Skogsmo

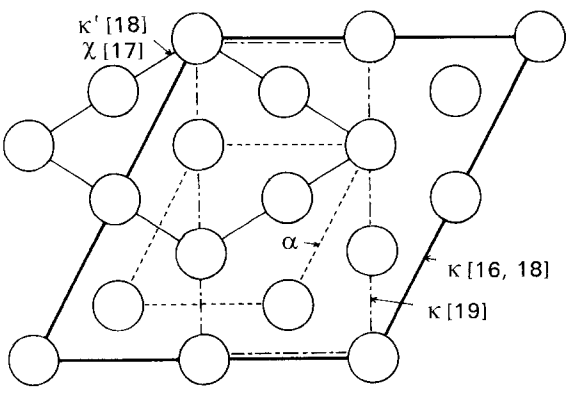

Figure 5 Relationship of unit cell of some aluminas with hexagonal-closed structure of oxygen. (○) Oxygen atoms; the plane of the figure shows the (0 0 0 1) plane.

TABLE II Comparison of the unit cell dimensions of the present whisker with those of some aluminas and an aluminium hydroxide with the structure of the h c p oxygen sublattice

	Structure	a (nm)	(b) (nm)	c (nm)	Space group	Ref.
Whisker of present work[a]	Hexagonal	0.562 (1 0 $\bar{1}$ 0)		1.72		
		0.974 (1 $\bar{1}$ 0 0)				
	Orthorhombic	0.487	–	1.72		
α	Rhombohedral	0.4758		1.2991	$D^6_{3D} - R\bar{3}c$	[14][b]
χ	Cubic	0.795				[15]
	Hexagonal	0.556		1.344		[16]
	Hexagonal	0.557		0.864		[17]
κ	Hexagonal	0.5544		1.786		[16][c]
	Hexagonal	0.167		–		[17]
	Hexagonal	0.9599		0.9015		[18]
	Orthorhombic	0.469	0.818	0.887	$Pna2_1$	[19]
κ′	Hexagonal	0.5544				[18]
Tohdite	Hexagonal	0.5575		0.8761	$P6_3mc$	[20]

[a] For estimation of the unit cell dimensions of the present whisker, the direction of streaking is considered to be c^*. In the hexagonal structure, the length of the a-axis is estimated for the two cases when the electron diffraction pattern are those on (1 0 $\bar{1}$ 0) and (1 $\bar{1}$ 0 0), respectively.
[b] The unit cell dimensions of α-alumina are those based on the hexagonal structure.
[c] The unit cell dimensions are derived from those for the orthohexagonal structure in the reference.

reported the crystal structure of κ-alumina [19]. They concluded that κ-alumina has the orthorhombic structure with the space group of $Pna2_1$, in which the oxygen sublattice is based on h c p. They also concluded that the structures determined by previous works are a superlattice of the orthorhombic κ-alumina structure. The oxygen sublattice of their κ-alumina, and, for comparison, that of κ-alumina reported by Saalfeld [16] and Okumiya *et al.* [18] are also shown in Fig. 5. The crystal structure of χ-alumina has been unclear. It is thought that the χ-phase is composed of the same oxygen sublattice as κ′-phase, as judged by the cell dimensions. The difference in crystal structure of the aluminas with an h c p oxygen lattice originates from that in the stacking sequence in the c-direction. α-alumina has the ABAB. . . stacking sequence and the unit cell is composed of the six closed-packed planes. On the contrary, κ′- and κ-aluminas have the ABAC. . . sequence and the unit cell composed of four close-packed oxygen planes [18, 19]. The occupation of aluminium ions in κ-alumina is the same as that of α-alumina, that is, aluminium cations occupy two-thirds of the octahedral interstices of the h c p oxygen lattice [19].

Fig. 6a shows the growth of whiskers on the surface of a spheroidized particle. The particle was melted and spheroidized in the Ar/N_2 plasma treatment. Fig. 6b is the surface morphology, where the very fine spherical particles and whiskers were ultrasonically separated in ethanol. The X-ray analysis of the spheroidized particles revealed the presence of α, γ, δ and θ-phases. It is clearly seen in Fig. 6b that the solidified traces develop in the symmetrical form on (0 0 0 1) of α-alumina, as indicated by A and B. The surface of the α-phase may provide the growth site for the whisker with the h c p oxygen sublattice.

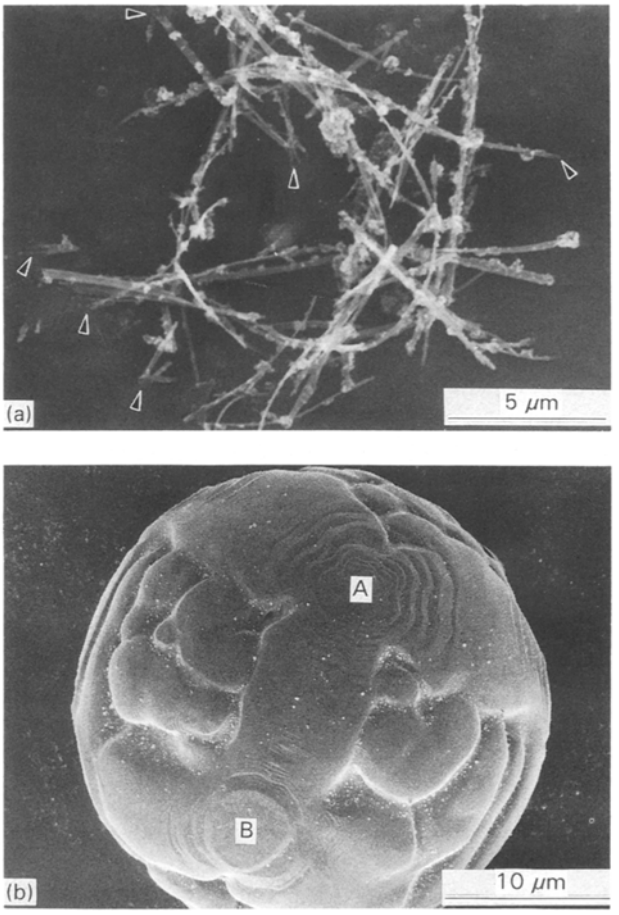

Figure 6 Surface morphology of a spheroidized alumina particle. (a) As shown by arrows, whiskers grow from the surface of the spheroidized particle. (b) The fine spherical particles and whiskers were removed ultrasonically. The solidification feature on the basal plane of the hexagonal structure is clearly seen.

The growth of whiskers requires some critical conditions in the vapour phase. Since Sears proposed the axial screw dislocation mechanism (ASD mechanism) for the growth of mercury whisker [21], it has been confirmed that some kinds of whisker grow by this mechanism. The growth of whiskers by the ASD mechanism requires moderate supersaturation in order to prevent two-dimensional nucleation. The other mechanisms, such as the vapour–liquid–solid mechanism (VLS mechanism) [22] and the twin formation

mechanism [23], were also proposed. There still remains the discrepancy in the growth mechanism for some whiskers; however, it is, at least, believed that the moderate supersaturation in the gas phase plays an important role in whisker growth. The growth of the present whiskers is related to the relatively low supersaturation in the vapour phase, and agrees with that of previously reported whiskers.

The streaking of electron spots in Fig. 3 is common in cases where the scattering domains of the form of thin sections, such as closely spaced faults or twins, or regular arrays of precipitates, are contained [24]. According to the kinematical theory of electron diffraction, the intensity distribution, $S(g_1g_2g_3)$, corresponding to a general parallelepiped of dimensions t_1, t_2, t_3 along the corresponding xyz directions is expressed as

$$S(g_1g_2g_3)^2 = \prod_{j=1}^{3} \frac{\sin^2 \pi t_j g_j}{(\pi a_j g_j)^2} \quad (4)$$

where g_1, g_2 and g_3 are the components of g at the reciprocal-lattice point, and a_1, a_2 and a_3 denote the unit-cell length, respectively. $t_j = N_j a_j$ where N_j is the number of unit cells along the domain edge j, s_j is the magnitude of the deviation vector, s, from the reflection sphere [24]. The interference regions for diffraction corresponding to these domains exhibit intensity spikes extended normal to the plane of the domains. The intersection of the reflection sphere with these intensity spikes then exhibits streaking. In the enlargement of a diffraction spot inset in the right-hand side of Fig. 3, a split of spikes can be seen. From Equation 4, the interval between the second and the third spikes from the centre is $1/t$ [25]. The thickness, t, of planar faults, which is parallel to the growth direction, is estimated to be about 18 nm. The thickness, 18 nm, corresponds to 60–70 layers of oxygen lattice.

The twin-related planar faults parallel to the c-axis were observed with a TEM in κ-alumina, which was deposited by means of chemical vapour deposition in the [0001] preferred direction of the hexagonal superlattice [26]. It has been reported that the prismatic faults are parallel to the c-axis in α-alumina [27], and that one of the growth directions of α-alumina whisker is [0001] [28]. Our data on the present whiskers agree with these aluminas, that is, the growth direction is in the c-axis and the planar faults are parallel to the c-axis.

5. Conclusion

The growth form of the deposits from the vapour phase varied depending on the plasma-generating and powder-feeding conditions. In all treatments with the Ar/H_2 and Ar/N_2 plasmas, very fine spherical particles below 200 nm diameter were formed. The fine particles consisted of metastable γ-, δ- and θ-phases. Some particles showed a faceted surface. Whiskers, 0.1–0.3 μm diameter and 5–15 μm long, were obtained in the Ar/N_2 plasma treatment at the powder feed rate exceeding 10 g min^{-1}. The structure was very similar to κ- or χ-aluminas with an hexagonal close-packed oxygen lattice. The variation is probably related to the difference in the supersaturation of the evaporated species.

Acknowledgements

The authors thank Mr M. Tsutsumi and Mr M. Yokoyama for help with the SEM and TEM observations, respectively.

References

1. T. ISHIGAKI and M. I. BOULOS, *Ceram. Trans.* **22** (*Ceram. Powder Sci.* **IV**), (1991) 139.
2. P. PROULX, J. MOSTAGHIMI and M. I. BOULOS, *Int. J. Heat Mass Transfer* **28** (1985) 1327.
3. *Idem, Plasma Chem. Plasma Process.* **7** (1987) 29.
4. B. LEWIS, in "Crystal Growth", 2nd. Edn edited by B. R. Pamplin (Pergamon Press, Oxford, 1980) p. 23.
5. J. HARVEY, H. I. MATTHEWS and H. WILMAN, *Discuss. Faraday Soc.* **30** (1960) 113.
6. T. I. BARRY, R. K. BAYLISS and L. A. LAY, *J. Mater. Sci.* **3** (1968) 229.
7. M. KAGAWA, F. HONDA, H. ONODERA and T. NAGAE, *Mater. Res. Bull.* **18** (1983) 1081.
8. K. WAFERS and G. M. BELL, "Oxides and Hydroxides of Aluminium", Technical Paper 19 (Alcoa Research Laboratories, Alcoa Center, PA, 1972).
9. M. SUZUKI, M. KAGAWA, Y. SYONO and T. HIRAI, *Ceram. Trans.* **22** (*Ceram. Powder Sci. IV*) (1991) 147.
10. S. IIJIMA, *Jpn J. Appl. Phys.* **23** (1984) L347.
11. G. LANTAGNE, B. MARCOS and B. CAYROL, *Comput. Chem. Eng.* **12** (1988) 589.
12. J. LOTHE and G. M. POUND, in "Nucleation", edited by A. C. Zettlemoyer, (Marcel Dekker, New York, 1969) p. 109.
13. R. McPHERSON, *J. Mater. Sci.* **8** (1973) 851.
14. ASTM Powder Diffraction File, 10–173 (American Society for Testing and Materials, Philadelphia, PA).
15. H. C. STUMPF, A. S. RUSSERLL, J. W. NEWSOME and C. M. TUCKER, *Ind. Eng. Chem.* **42** (1950) 1398.
16. H. SAALFELD, *N. Jb. Miner. Abh.* **95** (1960) 1.
17. G. W. BRINDLEY and J. O. CHOE, *Am. Mineral.* **46** (1961) 771.
18. M. OKUMIYA, G. YAMAGUCHI, O. YAMADA and S. ONO, *Bull. Chem. Soc. Jpn.* **44** (1971) 418.
19. P. LIU and J. SKOGSMO, *Acta Crystallogr.* **B47** (1991) 425.
20. G. YAMAGUCHI, H. YANAGIDA and S. ONO, *Bull. Chem. Soc. Jpn.* **37** (1964) 1555.
21. G. W. SEARS, *Acta Metall.* **3** (1955) 361.
22. R. S. WAGNER and W. C. ELLIS, *Appl. Phys. Lett.* **4** (1964) 89.
23. R. S. WAGNER and R. G. TREUTING, *J. Appl. Phys.* **33** (1961) 2490.
24. L. E. MURR, in "Electron Optical Applications in Materials Science" (McGraw-Hill, New York, 1970) pp. 254, 293.
25. P. B. HIRSCH, A. HOWIE, R. B. NICHOLSON and D. W. PASHLEY and M. J. WHWLAN, in "Electron Microscopy of Thin Crystals" (Butterworths, London, 1965) p. 98.
26. S. VUORINEN and J. SKOGSMO, *Thin Solid Films* **193/194** (1990) 536.
27. J. D. SNOW and A. H. HEUER, *J. Amer. Ceram. Soc.* **56** (1973) 154.
28. R. C. DeVRIES and G. W. SEARS, *J. Chem. Phys.* **31** (1959) 1256.

Received 24 August 1992
and accepted 11 January 1993